Variable Data Rate Architectures in Optical LEO Direct-to-Earth Links: Design Aspects and System Analysis

Pantelis-Daniel Arapoglou, Giulio Colavolpe, *Senior Member, IEEE*, Tommaso Foggi, Nicolò Mazzali, *Member, IEEE*, and Armando Vannucci

***Abstract*—In the frame of ongoing efforts between space agencies to define an on-off-keying-based optical low-Earth-orbit (LEO) direct-to-Earth (DTE) waveform, this paper offers an in-depth analysis of the Variable Data Rate (VDR) technique. VDR, in contrast to the currently adopted Constant Data Rate (CDR) approach, enables the optimization of the average throughput during a LEO pass over the optical ground station (OGS). The analysis addresses both critical link level aspects, such as receiver (time, frame, and amplitude) synchronization, as well as demonstrates the benefits stemming from employing VDR at system level.**

***Index Terms*—Free space optics, low Earth orbits (LEO) satellite communications, Variable Data Rate (VDR).**

I. Introduction

In RECENT years, optical communications have become increasingly appealing to the space industry. Beyond scientific experiments and demonstrations, new multi-year commercial missions resorting to optical links have emerged. For example, the European data relay system (EDRS) involves two geostationary satellites and tens of thousands of optical links materialized [1]. From low Earth orbits (LEO), direct-to-Earth (DTE) optical communications appeal not only to institutional missions (e.g., to download payload telemetry data of Earth observation missions), but can potentially have a significant commercial application [2].

Currently flying and planned optical LEO-DTE systems transmit at a constant data rate (CDR) while passing over an optical ground station (OGS) [3]. Such a transmit mode does not take into account the fact that the characteristics of the propagation channel may vary significantly during the satellite pass. Indeed, channel impairments like the free space loss, the atmospheric attenuation, and the turbulence of the refractive index of the atmosphere show a strong dependence on the satellite elevation angle [4]. In particular, the atmospheric turbulence, whose effect is known as scintillation, is the main source of fading that affects the optical signal [5]. Given such a high channel variability during the satellite pass, the CDR transmission mode requires a trade-off between two desirable but contrasting features: a high transmission data rate and a long satellite visibility window. Indeed, adopting a high data rate would require favourable channel conditions, typically available only at high elevation angles, which implies a reduced duration of the transmission window. On the other hand, a long transmission window requires the link closure at low elevation angles, that only low data rates would allow. Even when this trade-off is optimized, the CDR approach inevitably causes a significant throughput and data return loss compared to the theoretically available channel capacity.

An intuitive way to tackle this issue is a variable data rate (VDR) approach aiming at reducing the performance gap with respect to the channel capacity and, at the same time, allowing a longer visibility window. This can be achieved by splitting the pass of the LEO satellite in predefined sectors, and optimizing the data rate in each of them. The same concept is being already adopted, for example, by the next generation of Copernicus missions to download Earth observation data from LEO satellites on high data rate radio frequency (RF) links. In particular, the VDR concept is based in this case on the variation of the modulation order and of the rate of the forward error correcting (FEC) code [6]. However, in typical optical LEO-DTE waveforms, such as the one currently defined by the Consultative Committee for Space Data Systems (CCSDS) Optical Working group and referred to as Optical On-Off Keying (O3K), the modulation is fixed, hence it cannot be exploited as a degree of freedom to implement the VDR. In addition, the dynamic range offered by the variation of the FEC code rate alone turns out to be quite limited when compared to the link budget variability affecting the optical channel.

Other approaches to cope with variable channel conditions are of course possible, including ARQ-like strategies such as those adopted in [7] or in [8]. Such link-layer feedback protocols are especially needed when a high and constant data

Manuscript received 24 February 2022; revised 27 April 2022; accepted 14 May 2022. Date of publication 23 May 2022; date of current version 16 August 2022. *(Corresponding author: Armando Vannucci.)*

Pantelis-Daniel Arapoglou and Nicolò Mazzali are with the European Space Agency, European Space Research and Technology Centre, Radio Frequency Systems Division, 2200 AG Noordwijk, The Netherlands (e-mail: pantelis–daniel.arapoglou@esa.int; Nicolo.Mazzali@esa.int).

Giulio Colavolpe, Tommaso Foggi, and Armando Vannucci are with the Department of Engineering and Architecture, University of Parma, 43124 Parma, Italy, and also with the CNIT Research Unit, I-43124 Parma, Italy (e-mail: giulio.colavolpe@unipr.it; tommaso.foggi@unipr.it; armando.vannucci@unipr.it).

Color versions of one or more figures in this article are available at https://doi.org/10.1109/JLT.2022.3177244.

Digital Object Identifier 10.1109/JLT.2022.3177244

rate is adopted to exploit the short visibility window, like in NASA's TeraByte InfraRed Delivery (TBIRD) system, where large burst rates up to 200 Gbps are used [8]–[10]. Different possible implementations of the variable data rate paradigm have been proposed, both in coherent and in pulsed FSO transmission systems. In [11], the code rate and the modulation format are adjusted, for a coherent optical link. For pulsed optical systems, instead, a multi-rate optical transceiver was implemented in [12] with pulse position modulation, which achieves a very high sensitivity at the cost of decreased spectral efficiency. Adaptive rate optical terminals have been proposed and developed within the context of the NASA Laser Communications Relay Demonstration (LCRD) [13]–[16]. The multi-rate modems discussed in these papers are based on DPSK modulation, which differs from the OOK considered here and under current standardization, and their emphasis is on technology and on the development of a space grade terminal for GEO downlinks and possibly including adaptive optics (AO) and a large ground telescope. Hence, the sizing of the channel interleaver and its interplay with VDR were not investigated in [13]–[16]. Furthermore, the variable rate in [12]–[15] is realized by resorting to a variable duty-cycle approach that suffers from hardware non-idealities such as worse performance under higher extinction ratios or non-linearities appearing at very low duty-cycles.

The focus of this paper is instead on LEO downlink, with a low cost receiver without AO and small ground telescope. Thus, we put emphasis on waveform design, receiver synchronization and system benefits of VDR. The expected benefit in terms of throughput has already been forecast in previous works, mostly under ideal conditions and irrespective of the technological implementation. In [17], an improvement in throughput by a factor of 3 was obtained by assuming an ideally continuous adaptive data rate, without addressing issues related to the receiver design. In [18], similar throughput gains were achieved by ideally varying the symbol period (in a large but discrete set of values), in the presence of signal-dependent noise. A larger gain was shown to be achievable when the receiver is thermal-noise-limited and / or the transmitted power is employed as an extra degree of freedom.

In this paper, a novel way of implementing VDR in optical LEO-DTE on-off keying (OOK) waveforms is proposed, relying on the spreading of data in order to achieve the highest symbol rate allowed by the link budget in each sector of the satellite pass. In essence, the proposed VDR concept relies on transmitting always at a fixed chip rate and adapting the data rate by repeating/spreading each data symbol by a desired factor. Different flavours of VDR are possible [19], [20] but would require modifications of the hardware at both transmitter and receiver sides. For example, when the symbol rate is changed, synchronization has to be reacquired and, for this reason, only a few values of the symbol rate can be adopted, which results in a significant loss of data return. The proposed approach, instead, requires only digital baseband operations and the receiver architecture is not sensitive to the adopted spreading factor. In order to evaluate the average throughput gain brought about by VDR, we calculate the link budget by considering a specific OGS in Southern Italy, for which we assume a receiver employing an avalanche photodiode (APD) for the opto-electric conversion.

The intended contribution of this paper is twofold: first, we propose novel architectures that implement VDR in a hardware-efficient way, that shifts most of the complexity to the digital processing domain; second, all the technical issues for the implementation of the proposed architectures are discussed (in Section II and III), from the selection of spreading and pilot sequences to the details of synchronization and fading estimation algorithms, for which novel solutions are proposed.

The paper is organized as follows. The general design aspects, that apply to both CDR and VDR systems, are discussed in Section II. In particular, a possible transmitter and receiver architecture for a CDR system is described and a novel frame and timing synchronization procedure is discussed. Section III presents an overview of the proposed VDR concept along with a critical discussion on how to achieve it with appropriately selected spreading sequences. The necessary modifications to the transmitter and receiver architectures for a VDR system are also discussed in Section III. Section IV reports general physical layer simulation results with FEC coding and channel interleaving, used to cope with channel fading, thermal noise, and the shot noise generated by the APD. Section V presents a system level analysis of the gains offered by VDR in terms of average throughput, compared to the performance of CDR transmission. Finally, conclusions are drawn in Section VI.

II. General Design Aspects

A. System Model

We consider a free space optical (FSO) communication system employing the OOK modulation and assume that the receiver employs an APD [21], so that both thermal and shot noise have to be considered. In particular, the power spectral density (PSD) of the shot noise depends on the transmitted symbol, hence the sum of thermal and shot noise is modeled as a non-stationary additive Gaussian noise process. The received signal after the APD can thus be expressed as

$$r(t) = s(t - t_0; h, \boldsymbol{a}) + w(t - t_0) \tag{1}$$

where $s(t - t_0; h, \boldsymbol{a})$ and $w(t - t_0)$ are the useful signal and the noise process at the receiver, both affected by an unknown delay t_0 introduced by the channel. The useful signal can be expressed as

$$s(t; h, \boldsymbol{a}) = h \sum_k a_k p(t - kT) \tag{2}$$

being $\boldsymbol{a} = \{a_k\}$ the sequence of transmitted symbols[1] belonging to the alphabet $\{0, 1\}$, T the symbol time, and h an amplitude which is typically unknown as a consequence of the random

[1] Since the chosen modulation format is OOK, in the following we will use "bit" and "symbol" as synonyms.

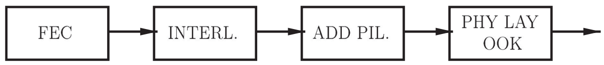

Fig. 1. Transmitter architecture.

nature of the scintillation and absorption phenomena characterizing an FSO link. We consider a non-return-to-zero (NRZ) transmission, where the duration of the rectangular shaping pulse $p(t)$, here assumed with unit energy, is one symbol period:

$$p(t) = \begin{cases} \frac{1}{\sqrt{T}} & 0 \le t < T \\ 0 & \text{otherwise.} \end{cases} \tag{3}$$

The noise process $w(t)$ in (1) can be expressed as

$$w(t) = w_{\text{th}}(t) + w_{\text{sh}}(t)\sqrt{T}\sum_k a_k p(t-kT)\,, \tag{4}$$

i.e., as the sum of the thermal noise $w_{\text{th}}(t)$, assumed to be white and Gaussian with two-sided PSD $N_0/2$, and of the independent shot noise $w_{\text{sh}}(t)$, still white and Gaussian, with two-sided PSD $N_{\text{sh}}/2$ (possibly depending on h). From (4), when a symbol "0" is transmitted, we have thermal noise only with PSD $N_0/2$, whereas when a symbol "1" is transmitted, the noise is the sum of $w_{\text{th}}(t)$ and $w_{\text{sh}}(t)$ with PSD $N_1/2 = (N_0 + N_{\text{sh}})/2$.

The unknown delay t_0 in (1) can be expressed as the sum of a component multiple of T plus a residual fractional delay τ, i.e.,

$$t_0 = k_0 T + \tau\,. \tag{5}$$

The above expression of t_0 is functional to the procedure adopted at the receiver to estimate the unknown delay. Indeed, the estimation of t_0 is performed in two separate steps, called *frame* and *timing synchronizations*, whose order depends on the chosen receiver architecture. In one step, the estimation of k_0 is performed by exploiting proper fields of known symbols, which yields a coarse alignment. In the other step, a *timing synchronization* algorithm has instead the task of estimating the fractional delay τ.

B. Transmitter and Receiver Architecture for Constant Data Rate

In order to perform frame and timing synchronization, as well as to estimate the value of h, we resort to a receiver architecture that performs data-aided (DA) estimation, hence we assume that blocks of P pilot symbols are periodically inserted in the transmitted data stream. When the channel coherence time is large, the distance between blocks of pilots can be chosen according to a maximum allowed overhead. Otherwise, the number of pilot fields and the distance between them has to be properly designed by addressing a trade-off between estimation accuracy and overhead minimization.

The transmitter architecture is shown in Fig. 1. The codewords at the output of the FEC channel encoder are interleaved by using a proper convolutional interleaver [22]. Interleaving is required since atmospheric turbulence is a slowly varying phenomenon with a very long coherence time. Pilot fields in blocks of P bits are then inserted and the resulting bit stream is then modulated using an OOK modulation with NRZ pulses.

The receiver architecture is reported in Fig. 2. After the APD (and the transimpedance amplifier, TIA, not reported in the figure), we assume that a matched filter (MF) is present. In general, we assume that N samples per symbol are extracted and processed at the output of the MF. *Frame synchronization* is performed first, by searching the correct alignment with the pilot fields.[2] DA *timing synchronization* is performed next, together with the estimation of the unknown amplitude h. The number of samples is then reduced, from N to only one sample per symbol, by interpolating the samples processed by the receiver. After pilot removal, the log-likelihood ratios are computed, deinterleaved, and passed to the decoder.

We seek algorithms able to perform DA frame and timing synchronization, with a trade-off between performance and complexity that privileges the simplicity of the receiver. As it is intuitive, at very low levels of received power P_{avg}, it is the thermal noise that dominates over shot noise. This conclusion can be confirmed not only by numerical simulation but also by the computation of theoretical bounds (such as the modified Cramér-Rao bound, MCRB), showing that the values computed with or without shot noise practically coincide when P_{avg} is very low.[3] Since this is indeed the low-power regime at which we expect the receiver to operate, we shall derive a synchronization algorithm under the assumption that only thermal noise is present. In any case, performance will be assessed, in the numerical results that follow, in a realistic scenario with both thermal and shot noise.

The receiver architecture described above has a major disadvantage: when the clock frequency is not stable and significantly changes over time or drifts due to the motion of a LEO satellite, a DA timing estimation algorithm is not able to track these variations if, between two consecutive pilot fields, they produce a slip of a symbol period (or a chip period in case of VDR, see Section III). The instability of the clock frequency is in practice a minor problem since sufficiently stable oscillators are nowadays available. As far as the motion effects are concerned, if the satellite knows its relative position with respect to the ground station, timing drifts can be precompensated at the transmitter. Otherwise, the only alternative is the use of a closed-loop non-data-aided (NDA) timing synchronization algorithm (possibly of the second order) able to track these variations.

We thus also consider a different receiver architecture, shown in Fig. 3, in which timing synchronization is performed in closed-loop NDA mode prior to any other receiver function. In particular, we will assume, for complexity reasons, that timing synchronization is performed by using at most $N \le 2$ samples per symbol. After timing synchronization and interpolation, the remaining functions are performed by using only one sample

[2]We assume that the channel coherence time is such that the channel can be considered as constant at least during a codeword length. Although, in general, more pilot fields can be employed to perform DA synchronization, we shall instead assume that the channel estimate, obtained by using a single pilot field, remains valid only for a codeword length.

[3]Such a theoretical investigation is however beyond the scope of the present work and will not be further addressed.

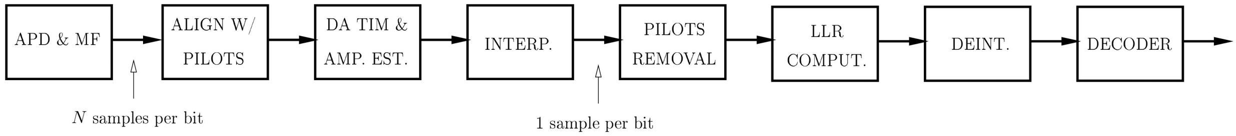

Fig. 2. Receiver architecture for DA timing synchronization.

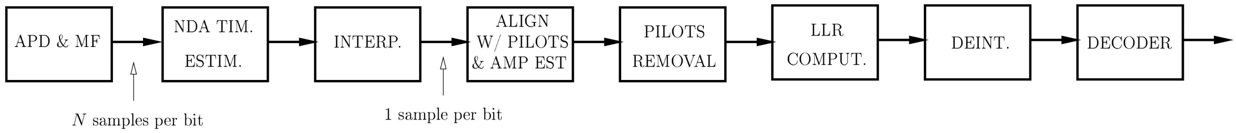

Fig. 3. Receiver architecture for NDA timing synchronization.

per symbol. In particular, the alignment with the pilot fields (i.e., frame synchronization) is performed jointly with amplitude estimation in DA mode, by using, for example, the algorithms described in [23]. After pilot removal, the log-likelihood ratios are then computed, deinterleaved, and passed to the decoder, as in the previous case.

Even in the case of NDA timing synchronization, we can adopt algorithms that were derived under the assumption that shot noise is absent. The same considerations indeed apply as in the case of DA timing synchronization, since receivers operate at very low values of P_{avg} where thermal noise is dominant over shot noise.

C. Frame and Timing Synchronization

Suppose to observe a chunk of the continuous-time received signal (1), with support $[\tilde{t}_0, \tilde{t}_0 + LT]$, where $L = P$ is chosen equal to the length of the pilot sequence.[4] The value $\tilde{t}_0$ is a tentative value of the actual channel delay t_0, that is assumed by the receiver and can be expressed as $\tilde{t}_0 = \tilde{k}_0 T + \tilde{\tau}$. We assume that the symbols in the observation window are known, as is the thermal noise PSD. On the contrary, the amplitude h is unknown and will be jointly estimated with timing; its tentative value at the receiver is denoted by $\tilde{h}$. The likelihood function for the joint estimation of t_0 and h, under the assumption that the shot noise is negligible, is [24]

$$\begin{aligned}\Lambda(\tilde{t}_0, \tilde{h}) =& \int_{\tilde{t}_0}^{\tilde{t}_0+LT} r(t) s(t - \tilde{t}_0; \tilde{h}, \boldsymbol{a}) dt \\ &- \frac{1}{2}\int_{\tilde{t}_0}^{\tilde{t}_0+LT} s^2(t - \tilde{t}_0; \tilde{h}, \boldsymbol{a}) dt \\ =& \int_{\tilde{t}_0}^{\tilde{t}_0+LT} r(t) \left[\sum_k \tilde{h} a_k p(t - kT - \tilde{t}_0)\right] dt \\ &- \frac{1}{2}\int_{\tilde{t}_0}^{\tilde{t}_0+LT} \left[\sum_k \tilde{h} a_k p(t - kT - \tilde{t}_0)\right]^2 dt \\ =& \tilde{h} \sum_{k=0}^{L-1} a_k x(kT + \tilde{t}_0) - \frac{1}{2}\tilde{h}^2 \sum_{k=0}^{L-1} a_k^2 \,, \end{aligned} \tag{6}$$

[4]In a more general setting, the observation window with length L symbols can be the union of different disjoint windows with length P symbols. Such a generalization to multiple pilot sequences is straightforward.

where

$$\begin{aligned} x(t) = \frac{1}{\sqrt{T}} \int_t^{t+T} r(\alpha) d\alpha = h \sum_k a_k g \\ \times (t - kT - t_0) + n(t - t_0) \end{aligned} \tag{7}$$

is the signal at the output of the MF. More precisely, $n(t - t_0)$ is the filtered noise while $g(t)$ is the triangular autocorrelation function of the rectangular transmission pulse $p(t)$. The maximum value of $g(t)$ is equal to 1, since we assumed $p(t)$ with normalized energy, then $g(t)$ linearly decays on both sides of the time origin. By defining the set of indices $\mathcal{K}_1 = \{k \in \{0, 1, 2, \ldots, L-1\} : a_k = 1\}$, corresponding to bits "1" in the sequence of L known symbols, and by $K_1 = |\mathcal{K}_1|$ their total number, (6) can be compactly expressed as

$$\Lambda(\tilde{t}_0, \tilde{h}) = \tilde{h} \sum_{k \in \mathcal{K}_1} x(\tilde{k}_0 T + kT + \tilde{\tau}) - \frac{1}{2}\tilde{h}^2 K_1 \,. \tag{8}$$

Samples $\{x(\tilde{k}_0 T + kT + \tilde{\tau})\}$ can be obtained by sampling the matched filter output, with symbol spacing and with a tentative delay $\tilde{t}_0 = \tilde{k}_0 T + \tilde{\tau}$. Defining their sum over $\mathcal{K}_1$ as

$$\Gamma(\tilde{k}_0, \tilde{\tau}) = \sum_{k \in \mathcal{K}_1} x(\tilde{k}_0 T + kT + \tilde{\tau}) \,, \tag{9}$$

the objective is to maximize it over the possible values of the delay, hence to estimate k_0 and τ as

$$(\hat{k}_0, \hat{\tau}) = \underset{\tilde{k}_0, \tilde{\tau}}{\operatorname{argmax}}\, \Gamma(\tilde{k}_0, \tilde{\tau}) \,. \tag{10}$$

Hence, the following estimate for the attenuation h,

$$\hat{h} = \frac{\Gamma(\hat{k}_0, \hat{\tau})}{K_1} \tag{11}$$

ensures that the likelihood function in (8) is maximized too. Note that there is an implicit ambiguity in the maximization in (10), since the choice for the pair $(\hat{k}_0, \hat{\tau})$ is equivalent to the choice, e.g., for $(\hat{k}_0 - 1, \hat{\tau} + T)$. This ambiguity is solved by constraining τ in an interval with duration T, such as $[0, T)$ or $[-T/2, T/2)$.

The procedure for frame and timing synchronization is performed in two separate steps. Recall that N samples per symbol are extracted at the output of the MF, which correspond to N different hypotheses for the values of $\tilde{\tau}$. Namely, N specific values $\tilde{\tau} + \tilde{n}\frac{T}{N}$ (with $\tilde{n} \in \{0, 1, \ldots, N-1\}$) are considered at the receiver. The frame synchronization step of the algorithm consists in a coarse search, in which we look for the maximum of Γ in a sliding window fashion. The search is performed with the constraint that $\tilde{\tau}$ takes one of the N considered values, hence the metric Γ is computed according to (9) by using L samples with spacing T.[5] The grid of L samples is then shifted in time by T/N at every step, by increasing the value considered for $\tilde{n}$ (or otherwise increasing $\tilde{k}_0$ and resetting $\tilde{n}$ to zero, when $\tilde{n} = N$). The frame synchronization step can be terminated by declaring that the alignment is found when the likelihood function exceeds a properly optimized threshold. When the alignment is declared, a verification step can be implemented by looking for other maxima in correspondence to the next pilot fields. This will help reducing the false alarm probability while the miss-detection probability can instead be reduced as much as required, by increasing L or otherwise by waiting for a sufficiently long time, since pilot fields are periodically inserted in the continuous transmitted stream. The symbols belonging to a pilot field need to belong to a sequence whose autocorrelation shows a clearly isolated maximum at the time origin. A very good choice, in this respect, is represented by the maximum length sequences or M-sequences [25].

The frame synchronization step yields not only the estimate $\hat{k}_0$ for the frame index but also a coarse timing estimate for τ, corresponding to the selected value $\hat{n}$ for $\tilde{n}$: we denote it by $\tau_1 = \tilde{\tau} + \hat{n}\frac{T}{N}$. If the frame synchronization is effective, then the residual error $\tau_1 - \tau$ lies within a sample interval, hence we can define a residual relative error $\varepsilon = (\tau_1 - \tau)/T \in [-1/(2N); 1/(2N)]$, and the metrics in (9) can be equivalently expressed with a single argument, as

$$\Gamma(\varepsilon) = h \sum_{k\in\mathcal{K}_1} \sum_{k'} a_{k'} g((k-k')T + \varepsilon T) + n(kT + \varepsilon T)\,, \tag{12}$$

where (7) is used to express the matched filter output $x(t)$. Considering that $g(t)$ extends in the interval $[-T; T]$, only two terms can contribute to the inner summation in (12), namely the symbols $a_{k\pm 1}$ next to a_k. Hence,

$$\begin{aligned}\Gamma(\varepsilon) &= h \sum_{k\in\mathcal{K}_1} \left[g(\varepsilon T) + a_{k-1} g((\varepsilon+1)T) + a_{k+1} g((\varepsilon-1)T)\right] \\ &\quad + n(kT+\varepsilon T) \\ &= h\left[(K_1 - K_{11}) g(\varepsilon T) + K_{11} g_{11}(\varepsilon T)\right] + n_1(\varepsilon T)\,,\end{aligned} \tag{13}$$

where $n_1(t) = \sum_{k\in\mathcal{K}_1} n(t + kT)$ is the sum of filtered noise samples affecting the "1" symbols and we defined $g_{11}(t) = g(t+T) + g(t) + g(t-T)$ as the sum of three adjacent autocorrelations (which is trapezoidal, in our case). In (13), we define K_{11} as the number of "11" subsequences in the known pilot field. The noiseless part of the metric $\Gamma(\varepsilon)$ in (13) can be computed, based on the autocorrelation $g(t)$ and its threefold version $g_{11}(t)$, as a function of the normalized error ε. Since the autocorrelation $g(t)$ is more peaked with respect to its smoother summed version $g_{11}(t)$, then it is easy to see that, for the purpose of timing estimation, a good pilot sequence is such that K_1 is much larger than K_{11}, so that the resulting metric $\Gamma(\varepsilon)$ reaches a sharp maximum around the zero of timing error ε.

The function $\Gamma(\varepsilon)$ should be maximized in the interval $\varepsilon = (\tau_1 - \tau)/T \in [-1/(2N); 1/(2N)]$. Within this interval, since $g_{11}(\varepsilon T)$ is constant in $(-1 \le \varepsilon \le 1)$, (13) has a triangular shape whose expression is

$$\Gamma(\varepsilon) = h\left[(K_1 - K_{11})(1 - |\varepsilon|) + K_{11}\right] + n_1(\varepsilon T)\,, \tag{14}$$

where, in the absence of noise, hK_1 is the maximum value of $\Gamma(\varepsilon)$ at $\varepsilon = 0$ and hK_{11} its minimum value at $\varepsilon = \pm 1$. These values depend on the pilot sequence, hence they are known at the receiver.

Let us shortly denote by $\Gamma_0 = \Gamma(\tilde{k}_0, \tau_1)$ the maximum of the metric in (9) that stems from frame synchronization, and by $\Gamma_{\pm\frac{1}{N}}$ the two neighbouring samples, corresponding to the metric computed at indices $(\tilde{k}_0, \tau_1 \pm \frac{T}{N})$. As stated, if frame synchronization is correct, then the time-continuous residual error εT lies in an interval $[-T/(2N); T/(2N)]$ with amplitude T/N. Let us suppose to have operated the frame synchronization algorithm with $N \ge 2$ samples per symbol interval. Γ_0 thus corresponds to the estimated start of the frame while $\Gamma_{-\frac{1}{N}}$ and $\Gamma_{\frac{1}{N}}$ are its neighbouring values, spaced by a fraction of the symbol period on both sides of Γ_0 (clearly, it is $\Gamma_0 > \Gamma_{\pm\frac{1}{N}}$) and we shall use the three values for the estimation of the residual timing error. Given the triangular profile (14) of $\Gamma(\varepsilon)$ within $(-1 \le \varepsilon \le 1)$, $N \ge 2$ samples per symbol ensure that, no matter where the maximum sample Γ_0 is located within the interval $\varepsilon \in [-1/2N; 1/2N]$, the following linear interpolation yields the maximum of (14):

$$\hat{\varepsilon} = \frac{1}{2N} \frac{\Gamma_{-\frac{1}{N}} - \Gamma_{\frac{1}{N}}}{\Gamma_0 - \min\{\Gamma_{-\frac{1}{N}}, \Gamma_{\frac{1}{N}}\}}\,. \tag{15}$$

This hence defines the estimate for the residual relative timing error. Note that in the case of a VDR system, timing estimation via (15) can be accomplished even by using $N = 1$ sample per symbol, provided that proper spreading sequences are employed, as further discussed in Section III-B.

The estimate of τ is finally obtained as

$$\hat{\tau} = \tau_1 - \hat{\varepsilon} T\,.$$

The maximum of the metric in (14) can be equally expressed in an easy way, resorting to the triangular shape of $\Gamma(\varepsilon)$, in terms of the three samples above,

$$\Gamma_{\max} = \Gamma_0 + \frac{1}{2}\left|\Gamma_{-\frac{1}{N}} - \Gamma_{\frac{1}{N}}\right| \tag{16}$$

and, from this, the amplitude estimation can be found from the general relationship (11):

$$\hat{h} = \frac{\Gamma_{\max}}{K_1}\,. \tag{17}$$

Besides the DA timing and amplitude estimation described above, the receiver can adopt a NDA timing estimation that is performed first, according to the architecture reported in Fig. 3. Frame synchronization, i.e., the alignment with the pilot field, as

[5]As mentioned, in a more general setting the L samples do not need to correspond to a single pilot field but more fields can be employed if the channel coherence time is sufficiently long.

well as amplitude estimation can be performed at a subsequent stage, after interpolation and downsampling, by using only one sample per symbol [23]. For the timing synchronization, one of the traditional algorithms proposed in the literature can be used. In the numerical results described in Section IV, we compare the NDA early-late detector (ELD) technique with that proposed by Gardner [24], both achieving good performance in the considered system scenario. Note that we only consider schemes based on digital signal processing, neglecting highly suboptimal clock recovery schemes that are based on an analog circuitry, as those described in [26], [27].

III. Variable Data Rate System Design

A. The Variable Data Rate Concept

The proposed VDR approach is based on the assumption that the OOK modulation scheme is used, which is particularly suitable for low-complexity optical LEO-DTE communications [28]. In addition, OOK is the modulation format of choice in the ongoing CCSDS standardization of the optical LEO-DTE physical layer, referred to as O3K [29]. In particular, to cater for a variety of system configurations, the O3K standard allows for a wide set of symbol rates, ranging from around 1.2 Msym/s to 10 Gsym/s.

Despite such a wide range of symbol rates, the current concept of operations (ConOps) for optical typical LEO-DTE links has been to select only one of them and transmit at a CDR during the pass over the OGS. This approach, as discussed in the introduction, is clearly suboptimal. Instead, the VDR-based ConOps relies on splitting the pass in a predefined set of sectors, and selecting the optimal symbol rate for each of them in a pre-programmed manner. The symbol rate is thus selected so as to close the link under the different channel conditions experienced during a pass. The available channel capacity is thus incrementally exploited as the channel conditions improve.

The proposed method to seamlessly change the symbol rate during the pass is to spread the data symbols to the highest possible chip rate the transmit or receive hardware can support. Since both transmitter and receiver always operate at a constant chip rate, the VDR is implemented by changing the spreading factor in each sector of the pass, so that the underlying symbol rate matches the selected symbol rate for each sector.

While the idea of VDR is not new per se, the implementation proposed here allows a straightforward extension of the novel reception techniques discussed in Section II (synchronization and fading estimation algorithms) from CDR to VDR system. In addition, the data spreading technique adopted here calls for a detailed analysis of the spreading sequances to be adopted, which we discuss next.

B. Selection of the Spreading Sequences

The VDR technique foresees the use of spreading sequences to represent the bits “0” and “1”. The chip rate is kept constant whereas the symbol rate is decreased by increasing the length of the spreading sequences. In other words, we may express the transmitted signal as

$$s(t) = \sum_k \sum_{m=0}^{M-1} s_m(a_k) p\left[t - (kM+m)T_c\right]$$

where $[s_0(a), s_1(a), \ldots, s_{M-1}(a)]^T$ is the spreading sequence associated with bit $a \in \{0,1\}$, composed of binary symbols belonging to the alphabet $\{0,1\}$. M is the length of the spreading sequence, T_c is the chip time, and $p(t)$ is a rectangular pulse with unit energy and duration T_c, i.e.,

$$p(t) = \begin{cases} \frac{1}{\sqrt{T_c}} & 0 \le t < T_c \\ 0 & \text{otherwise}\,. \end{cases} \tag{18}$$

Regarding the length M of the spreading sequence, it is assumed that the possible values are $M = 2^0, 2^1, 2^2, \ldots$ We assume perfect synchronization at the receiver. The signal at the output of a filter matched to the pulse $p(t)$ is sampled at time instants $(iM+\ell)T_c$ obtaining the samples

$$x_{iM+\ell} = h s_\ell(a_i) + n_{iM+\ell} \tag{19}$$

where h is the channel attenuation, taking into account the atmospheric turbulence, and $\{n_{iM+\ell}\}$ are zero-mean independent random variables with variance $\sigma^2(s_\ell) = \sigma_0^2(1-s_\ell) + \sigma_1^2 s_\ell$, where $\sigma_0^2 = \frac{N_0}{2}$ and $\sigma_1^2 = \frac{N_1}{2}$. These samples will be used to compute the log-likelihood ratios (LLRs) to be sent to the decoder. The LLR for symbol a_i can be computed as

$$\begin{aligned}\lambda(a_i) &= \ln \frac{\prod_{\ell=0}^{M-1} p(x_{iM+\ell}|a_i=1)}{\prod_{\ell=0}^{M-1} p(x_{iM+\ell}|a_i=0)} \\ &= \sum_{\ell=0}^{M-1} \ln p(x_{iM+\ell}|a_i=1) - \sum_{\ell=0}^{M-1} \ln p(x_{iM+\ell}|a_i=0) \\ &= \frac{1}{2}\sum_{\ell=0}^{M-1}\left\{ \ln \frac{\sigma_0^2[1-s_\ell(0)] + \sigma_1^2 s_\ell(0)}{\sigma_0^2[1-s_\ell(1)] + \sigma_1^2 s_\ell(1)} \right. \\ &\quad - \frac{[x_{iM+\ell} - h s_\ell(1)]^2}{\sigma_0^2[1-s_\ell(1)] + \sigma_1^2 s_\ell(1)} \\ &\quad \left. + \frac{[x_{iM+\ell} - h s_\ell(0)]^2}{\sigma_0^2[1-s_\ell(0)] + \sigma_1^2 s_\ell(0)} \right\}\end{aligned} \tag{20}$$

i.e., as the sum of the LLRs associated with each chip.

The first problem to be solved is related to the selection of the spreading sequences. From (20), we can easily observe that, if for some ℓ we select $s_\ell(0) = s_\ell(1)$, the corresponding contribution of $x_{iM+\ell}$ to the LLR will be zero and this will produce a performance loss since that sample is not exploited for detection/decoding. Hence, the two spreading sequences corresponding to “1” and “0” must be complementary and we can simply provide one of them (for example the one corresponding to the bit “1”).[6] We will select $s_\ell(1) = s_\ell$ and $s_\ell(0) = \overline{s}_\ell = 1 - s_\ell$, i.e., $\overline{s}_\ell$ is the bit complementary to s_ℓ. With this choice, the LLR

[6]We shall assume in the following that, for a given M, σ_0 and σ_1 do not depend on the choice of M_1, i.e., on the spreading sequence. We will see in Section IV-B that this could not be the case.

can be expressed as

$$\lambda(a_i) = \frac{1}{2}\sum_{\ell=0}^{M-1}\left\{\ln\frac{\sigma_0^2 s_\ell + \sigma_1^2(1-s_\ell)}{\sigma_0^2(1-s_\ell)+\sigma_1^2 s_\ell} - \frac{[x_{iM+\ell}-hs_\ell]^2}{\sigma_0^2(1-s_\ell)+\sigma_1^2 s_\ell} + \frac{[x_{iM+\ell}-h(1-s_\ell)]^2}{\sigma_0^2 s_\ell + \sigma_1^2(1-s_\ell)}\right\}. \tag{21}$$

Considering the fact that the LLR is given by the sum of independent contributions, we can also state that the performance of a pair of spreading sequences (that for bit "1" and the complementary spreading sequence for bit "0") will depend on the number M_1 ($0 \le M_1 \le M$) of chips "1" in the spreading sequence corresponding to bit "1," and will be independent of their position. Our aim is thus to select the value of M_1 which maximizes the performance.

Without loss of generality, we will assume that the spreading sequence corresponding to bit "1" is as follows

$$\boldsymbol{s}(1) = [s_0(1), s_1(1), \ldots, s_{M-1}(1)]^T = [\underbrace{1,\ldots,1}_{M_1},\underbrace{0,\ldots,0}_{M-M_1}]^T.$$

As a consequence, the spreading sequence corresponding to bit "0" will be

$$\boldsymbol{s}(0) = [s_0(0), s_1(0), \ldots, s_{M-1}(0)]^T = [\underbrace{0,\ldots,0}_{M_1},\underbrace{1,\ldots,1}_{M-M_1}]^T.$$

As mentioned, when transmitting the bit a_i (where a_i can be either "0" or "1"), the samples $\{x_{iM+\ell}\}$ can be expressed as (19) where the variance of $n_{iM+\ell}$ is $\sigma_0^2[1-s_\ell(a_i)]+\sigma_1^2 s_\ell(a_i)$. We thus have a memoryless channel with input a_i and vector output

$$\boldsymbol{x}_i = [x_{iM+0}, x_{iM+1}, \ldots, x_{iM+M-1}]^T.$$

Considering that we foresee the use of a capacity achieving error correcting code, we look for the value of M_1 which maximizes the mutual information

$$I(A;\boldsymbol{X}) = \mathrm{h}(\boldsymbol{X}) - \mathrm{h}(\boldsymbol{X}|A)$$

where the differential entropies $\mathrm{h}(\boldsymbol{X})$ and $\mathrm{h}(\boldsymbol{X}|A)$ are defined as

$$\mathrm{h}(\boldsymbol{X}) = -\int p(\boldsymbol{x}_i)\log_2 p(\boldsymbol{x}_i)d\boldsymbol{x}_i$$

$$\mathrm{h}(\boldsymbol{X}|A) = -\sum_{a_i\in\{0,1\}}\int p(\boldsymbol{x}_i|a_i)P(a_i)\log_2 p(\boldsymbol{x}_i|a_i)d\boldsymbol{x}_i$$

where $P(a_i) = \frac{1}{2}$ is the a-priori probability of the input symbols, $p(\boldsymbol{x}_i|a_i)$ is the conditional probability density function (PDF) of the output given the input, and $p(\boldsymbol{x}_i)$ is the output PDF. The entropy $\mathrm{h}(\boldsymbol{X}|A)$ can be computed in closed form and it can be easily verified that it is independent of M_1. Thus the problem can be restated as the search for the value of M_1 which maximizes the entropy $\mathrm{h}(\boldsymbol{X})$. The pdf $p(\boldsymbol{x}_i)$ can be expressed as

$$p(\boldsymbol{x}_i) = \frac{1}{2}p(\boldsymbol{x}_i|a_i=0) + \frac{1}{2}p(\boldsymbol{x}_i|a_i=1) \tag{22}$$

where, considering the structure of $\boldsymbol{s}(0)$ and $\boldsymbol{s}(1)$

$$p(\boldsymbol{x}_i|a_i=0) = \left(\frac{1}{\sqrt{2\pi\sigma_0^2}}\right)^{M_1}\left(\frac{1}{\sqrt{2\pi\sigma_1^2}}\right)^{M-M_1} \times\exp\left\{-\frac{1}{2\sigma_0^2}\sum_{\ell=0}^{M_1-1}x_{iM+\ell}^2 - \frac{1}{2\sigma_1^2}\sum_{\ell=M_1}^{M-1}[x_{iM+\ell}-h]^2\right\}$$

$$p(\boldsymbol{x}_i|a_i=1) = \left(\frac{1}{\sqrt{2\pi\sigma_1^2}}\right)^{M_1}\left(\frac{1}{\sqrt{2\pi\sigma_0^2}}\right)^{M-M_1} \times\exp\left\{-\frac{1}{2\sigma_1^2}\sum_{\ell=0}^{M_1-1}[x_{iM+\ell}-h]^2 - \frac{1}{2\sigma_0^2}\sum_{\ell=M_1}^{M-1}x_{iM+\ell}^2\right\}.$$

Unfortunately, the entropy $\mathrm{h}(\boldsymbol{X})$ cannot be expressed in closed form. However, it can be numerically computed for any value of σ_0^2, σ_1^2, and h, resorting to the following procedure.

Considering that $\lambda(a_i)$ is an alternative sufficient statistic, the data processing inequality [30] ensures that $I(A;\boldsymbol{X}) = I(A;\Lambda)$. This can be easily demonstrated considering that

$$\prod_{\ell=0}^{M-1}p(x_{iM+\ell}|a_i=1) = \frac{e^{\lambda(a_i)}}{1+e^{\lambda(a_i)}} = \frac{1}{1+e^{-\lambda(a_i)}}$$

$$\prod_{\ell=0}^{M-1}p(x_{iM+\ell}|a_i=0) = \frac{1}{1+e^{\lambda(a_i)}}.$$

By defining the function

$$w(x) = \frac{1}{1+e^x}\ln\frac{2}{1+e^x} + \frac{1}{1+e^{-x}}\ln\frac{2}{1+e^{-x}},$$

we can compute $I(A;\Lambda)$ as

$$I(A;\Lambda) = E[w(\lambda)] \simeq \frac{1}{K}\sum_{k=0}^{K-1}w[\lambda(a_k)] \tag{23}$$

i.e., through a time average over a transmitted sequence of proper length K.[7]

The conclusion is that for the values of σ_0^2, σ_1^2, and h at hand, and in the range of values of P_{avg} of interest, we always found that the optimal value of M_1 is $M_1 = M$ (or equivalently $M_1 = 0$). The best possible spreading sequences to be associated with bits "0" and "1" are thus

$$\boldsymbol{s}(0) = [0,0,\ldots,0]^T$$

$$\boldsymbol{s}(1) = [1,1,\ldots,1]^T. \tag{24}$$

This choice is conceptually equivalent to reducing the symbol rate by enlarging the transmission pulse duration by a factor M.

[7] In the numerical results, the computed mutual information will be used to show the theoretical limits in the reported bit error rate curves.

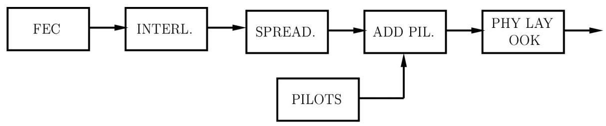

Fig. 4. VDR transmitter.

As a consequence, the duration of each coded bit is M times longer even at the output at the matched filter, so that the profile of the metrics in (13) is scaled in time by the same amount and DA timing estimation via (15) can be accomplished by using only $N = 1$ sample per chip, whenever $M \geq 2$.

On the other hand, there are different sequences to be preferred from different points of view. As an example, if a NDA timing estimation algorithm is selected, it is more convenient to increase the number of symbol transitions. Thus, from this point of view the best possible spreading sequences are

$$\begin{aligned} \boldsymbol{s}(0) &= [0, 1, 0, 1, \ldots, 0, 1]^T \\ \boldsymbol{s}(1) &= [1, 0, 1, 0, \ldots, 1, 0]^T . \end{aligned} \tag{25}$$

In the following, we will refer to a scheme employing the spreading sequences (24) as "scheme 1," whereas a scheme using the spreading sequences (25) will be referred to as "scheme 2".

C. Transmitter and Receiver Architecture for Variable Data Rate

In the case of VDR, the transmitter architecture is depicted in Fig. 4. Compared to the one considered in Section II-B for CDR, a spreading of the coded bits is present, as discussed in Section III-B. Since the larger the value of M, the lower the value of P_{avg}, it is intuitive that in the case of spreading we will need more pilots to perform a proper estimate of the unknown parameters. On the other hand, if we apply the spreading to the pilot fields too, we could destroy their autocorrelation properties, as will be discussed in the following.

At the receiver side, we report two possible architectures, depending on the way in which timing synchronization is performed. In particular, the VDR receiver architecture based on DA timing synchronization is shown in Fig. 5. Compared to the DA receiver architecture for CDR in Fig. 2, there is an estimation of the spreading factor, performed jointly with pilot alignment, and the LLR computation is performed by using (21). Regarding the number N of samples per chip, given the increased sample frequency due to the spreading, we shall assume at most $N = 2$ in the following. A VDR receiver architecture envisaging NDA timing synchronization is shown in Fig. 6. As discussed in Section II-B, although timing synchronization is performed in closed-loop NDA mode, the other parameters are estimated in DA mode using pilots.

Let us address again the choice of the spreading factor, this time not from the point of view of the bit error rate (BER), but from the point of view of the estimation performance. In case of adoption of the NDA architecture, as already stated, the best choice for the spreading sequence is represented by the "scheme 2". On the other hand, this spreading sequence, if applied to a pilot field with the aim of obtaining a longer pilot field, will destroy the autocorrelation properties of the M-sequence. As a consequence, in this case it is better to avoid spreading the pilot field. On the contrary, when the payload is spread by a factor of M, we need to adopt a different pilot field with length LM, where L is the length of the pilot field in the absence of spreading. At the receiver side, after NDA timing estimation, interpolation, and downsampling, we have to perform the alignment with pilots (i.e., frame synchronization), amplitude estimation, and the estimation of the spreading factor. In a LEO-DTE link, the spreading factor employed will be a deterministic function of the elevation angle. Hence, we can imagine that the OGS adopts a geometry-based method [31] to predict the employed spreading factor with, at most, an uncertainty between two possible adjacent values, e.g., M and $2M$. The receiver has to evaluate the correlation with both pilot fields having length M and $2M$. This will allow the receiver to perform both frame synchronization and, implicitly, the estimation of the spreading factor. Once frame synchronization has been performed, DA amplitude estimation can be carried out. A possible way to avoid multiple correlations is the adoption of properly designed pilot fields, such that the pilot field with length LM coincides with the first half of the pilot field with length $2LM$. In this way, it would be sufficient to correlate the received signal with the longer sequence and, from the obtained maximum value of the correlation, one could understand if the alignment is obtained with the shorter or the longer sequence. The details of this procedure are omitted for brevity.

Let us now consider the DA architecture in Fig. 5. In this case, considering that the different spreading sequences have a limited impact on the BER performance, and since timing synchronization is performed in DA mode using the pilot field, we can generate a longer pilot field by spreading the original pilot field that is used in the absence of spreading. In order to simplify the transmitter, the same spreading sequences can then be used for the payload too. We thus wish to investigate the impact of different spreading sequences, as applied to obtain a longer pilot field, on DA frame, timing, and amplitude estimation. We shall consider the following scenarios:

- *Scenario 1:* In the presence of spreading, with a spreading factor M, we obtain a longer pilot field by spreading with "scheme 1" the pilot field sequence, which in the absence of spreading has length L.
- *Scenario 2:* In the presence of spreading, with a spreading factor M, we obtain a longer pilot field by spreading with "scheme 2" the pilot field sequence, which in the absence of spreading has length L.
- *Scenario 3:* In the presence of spreading, with a spreading factor M, we obtain a longer pilot field by spreading the pilot field sequence, which in the absence of spreading has length L, with an M-sequence with length M and its complementary sequence.[8]

[8]M-sequences have length $2^P - 1$ with P a proper integer [25]. On the contrary, the spreading factors M are always a power of two. For this reason we appended a bit "0" to the generated M-sequence. Given the spreading factor M, we always employed binary M-sequences shifted by two steps and using a second set of weights, as explained in [32].

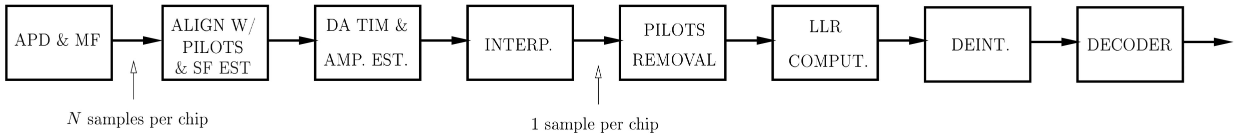

Fig. 5. VDR receiver architecture for DA timing synchronization.

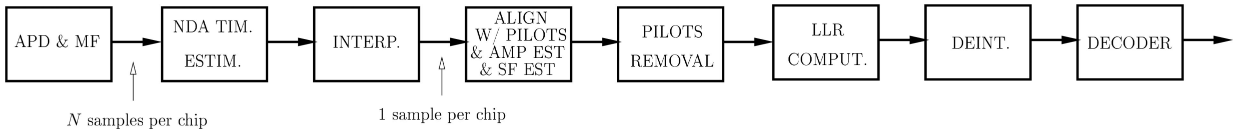

Fig. 6. VDR receiver architecture for NDA timing synchronization.

- *Scenario 4:* In the presence of spreading, with a spreading factor M, we obtain a longer pilot field by using a new M-sequence with length $L' = (L+1)M - 1$, instead of the length L that was used in the absence of spreading.

It is worth highlighting that scenarios 3 and 4 were obtained by using M-sequences, which have intrinsically excellent correlation properties, therefore better performances are expected in terms of miss-detection. Moreover, the first three schemes show the advantage that different pilot fields do not need to be stored at both transmitter and receiver. In the numerical results in Section IV we shall compare the four scenarios above.

IV. Link Level Numerical Results

A. Receiver With Fixed Bandwidth

Since the OOK transmitter uses intensity modulation, we assume that the average received optical power P_{avg} implicitly accounts (among others) for the attenuating effect of turbulence. When a bit "1," is received, the receiver APD, with responsivity R and multiplication factor M_P, yields an average current equal to $2P_{\text{avg}}RM_P$. We set

$$h = 2P_{\text{avg}}RM_P\sqrt{T_c}$$

so as to account for the gain of the normalized transmission pulse (18). The one-sided PSD of thermal noise current is

$$N_0 = \frac{4kT_0}{R_L}, \tag{26}$$

where kT_0 is the receiver temperature times the Boltzmann's constant ($k = 1.3806 \cdot 10^{-23}$ J/K) and R_L is the APD's load resistance. When the APD is followed by a transimpedance amplifier (TIA), as is assumed here, the dominant source of thermal noise is the TIA's feedback resistor, hence we assume that it coincides with R_L. Note that the TIA's feedback resistor R_L also determines the bandwidth of the receiver: by a simple single-pole approximation, $B = (2\pi R_L C_L)^{-1}$, where C_L is the APD's load capacitance (including both the input capacitance and a possible feedback capacitor of the TIA). The one-sided PSD of shot noise can be expressed as [33]

$$N_{\text{sh}} = 4eM_P{}^2FRP_{\text{avg}} \tag{27}$$

TABLE I
APD and TIA Parameters

Parameter	Value
R_L	160 Ω
C_L	0.2 pF
T_0	290 K
F	5
R	0.9 A/W
M_P	20

where F is the APD excess noise factor and e is the electron charge ($1.60217662 \cdot 10^{-19}$ C).[9] In the numerical results that follow, we use a chip rate of 10 Gchip/s and the APD and TIA parameters in Table I, so that the receiver bandwidth is fixed at half the chip rate ($B = (2T_c)^{-1}$) and the thermal current density, from (26), is $i_{\text{th}} = \sqrt{N_0} \simeq 10^{-11}$ A/$\sqrt{\text{Hz}}$.

In the following, separated results on the different estimation algorithms and BER performance, given the proposed spreading sequences, will be presented, so that each technique can be properly evaluated. This way, a useful benchmark for each one of the proposed techniques will be provided.

Considering the receiver architecture in Fig. 5 for VDR transmission in the case of DA timing synchronization, we evaluated its performance. Regarding the performance of frame synchronization, we first considered its evaluation in terms of miss-detection probability, defined as the probability that the timing estimation error exceeds $T/2$, i.e., $P(|\tau - \hat{\tau}| > T/2)$. Fig. 7 reports the results for the proposed algorithm, by first considering a system without any spreading sequence, where a pilot field with length $L = 511$ is employed.[10] Performance is compared to that of a VDR system where a spreading factor $M = 16$ is adopted and the four different scenarios described

[9]Note that in [33] an integrate-and-dump (I&D) filter, with gain $(eM_P)^{-1}$ and time extension equal to the pulse duration T_c, is assumed to follow the APD, so that each PSD (or noise variance) is multiplied by $T_c/(eM_P)^2$, while signal samples include a multiplying factor $T_c/(eM_P)$. We did not account for an I&D filter so that the parameter values in this section apply to continuous-time signals.

[10]This means that the spreading was obtained by using a M-sequence with length 15 for scenario 3, and with length $L' = 8191$ for scenario 4 (both with a "0" padded at the end).

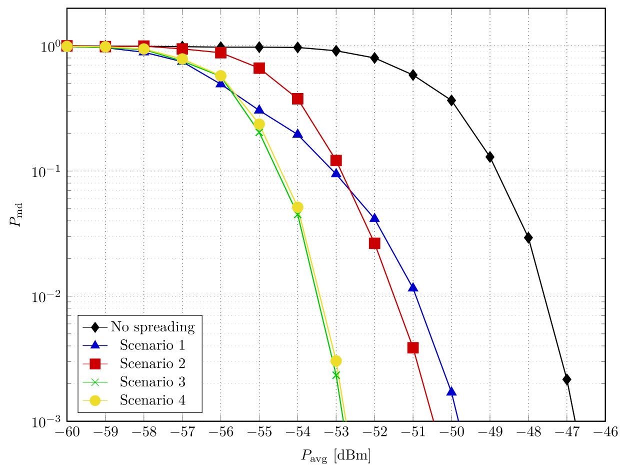

Fig. 7. Miss-detection probability. The original pilot field length is $L = 511$ and the spreading factor is $M = 16$.

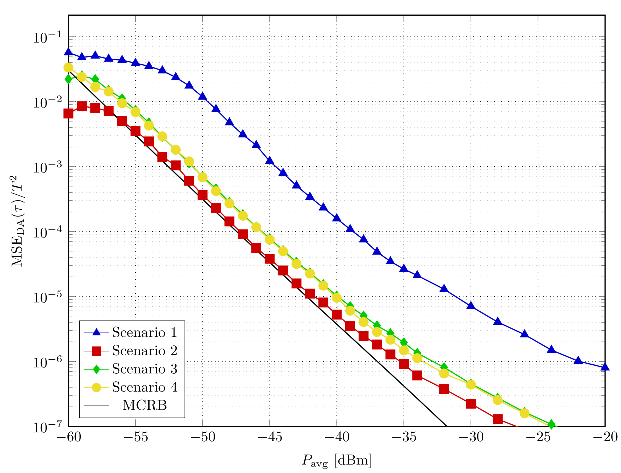

Fig. 8. Performance for timing estimation. The spreading factor is $M = 16$.

in Section III-C are considered for the spreading strategy. A significant gain of more than 6 dB is observed, in scenarios 3 and 4, with respect to the case where no spreading is present. On the other hand, scenario 2 provides the worst performance within the VDR framework. Indeed, in this case the adopted spreading sequences destroy the autocorrelation properties of the M-sequence employed as pilot field, as expected.

Moving to timing synchronization, Fig. 8 reports the estimation results in terms of normalized timing mean squared error (MSE) versus P_{avg}. The four scenarios are again considered in the case of a spreading factor $M = 16$. In this case, scenario 1 is the worst, as expected. Indeed, the number of $0 \rightarrow 1$ and $1 \rightarrow 0$ transitions is the same as in the absence of spreading, so that a spreading gain cannot be expected. On the contrary, scenario 2 is the best one since, in this case, the number of transitions is maximized.

Finally, all four scenarios are equivalent in terms of amplitude estimation, as shown in Fig. 9. As a conclusion, taking into account both timing and frame synchronization, as well as amplitude estimation, scenarios 3 and 4 must be preferred.

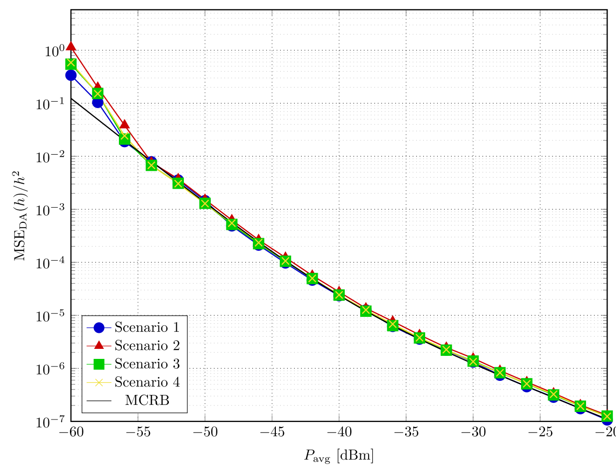

Fig. 9. Performance for amplitude estimation.

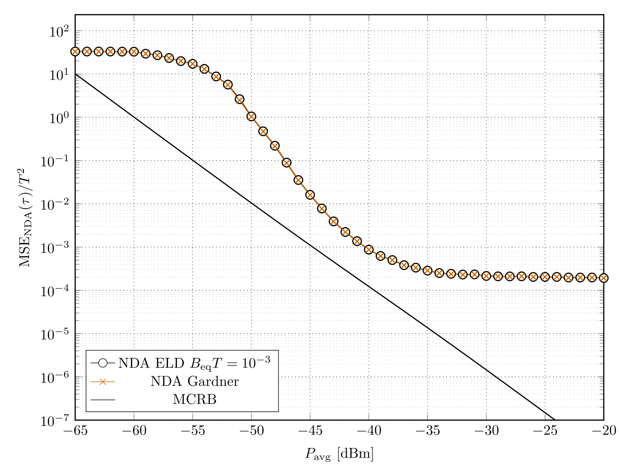

Fig. 10. Performance of the NDA ELD and of the NDA Gardner algorithms for timing estimation in the case of a CDR system ($B_{\mathrm{eq}}T = 10^{-3}$).

If synchronization is instead performed in a NDA fashion, we can consider the simple receiver architecture in Fig. 3 for CDR transmission, where timing estimation can be accomplished by traditional NDA algorithms that do not require the knowledge or the estimate of the amplitude h. Fig. 10 shows the performance of two such algorithms in terms of normalized timing estimation MSE versus P_{avg}. More precisely, the NDA ELD and the NDA technique proposed by Gardner [24] are compared, showing an almost identical performance, when the normalized equivalent bandwidth is set to $B_{\mathrm{eq}}T = 10^{-3}$. Along with simulation results, Fig. 10 shows the MCRB computed for the considered system, so as to highlight the margin of the achieved performance with respect to the theoretical limit.

As a further step, we analyzed and compared the error rates of CDR and VDR systems, focusing in particular on the impact of the spreading factor M, where $M = 1$ can be seen as a degenerate case of VDR coinciding with a CDR system, assuming perfect synchronization in order to show a fair comparison for the impact of different spreading schemes on the BER. Fig. 11 reports the BER performance versus P_{avg} obtained on an additive white Gaussian noise (AWGN) channel by using a FEC code (a serially concatenated convolutional code, SCCC, [34] with

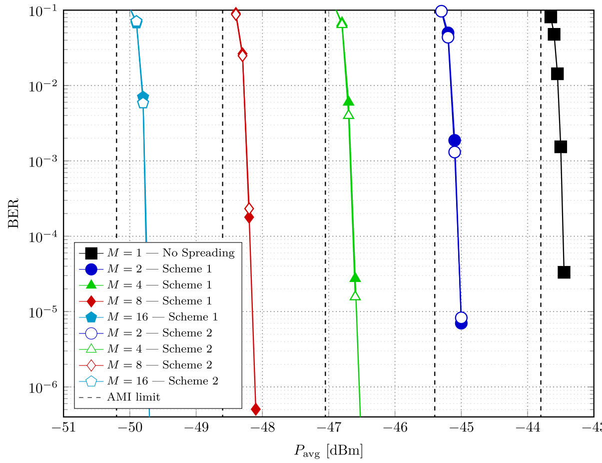

Fig. 11. BER performance on AWGN channel for schemes 1 and 2 and a few different spreading factors. A SCCC [34] with code rate 0.46 is considered.

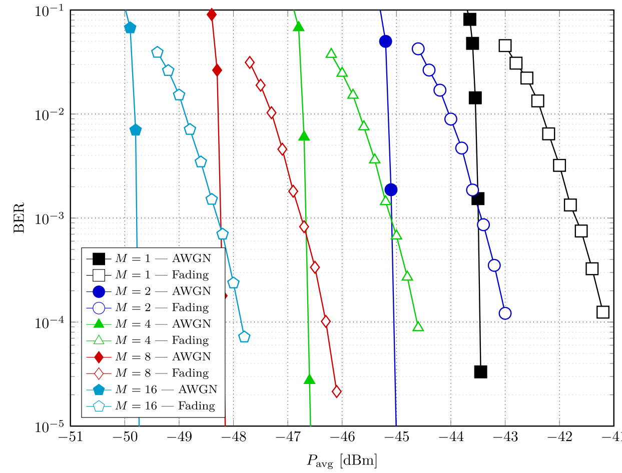

Fig. 12. BER performance on AWGN and turbulent fading channels (PSI= 0.1), for a few different spreading factors. Results are not sensitive to the adopted spreading scheme.

code rate 0.46), when employing the two spreading schemes introduced in Section III-B and different values of the spreading factor M. A convolutional interleaver was employed, along with one of the fading time series presented in [35] (in particular, the time series marked as A). It can be observed that, while the two spreading schemes deeply affect DA frame and timing synchronization procedures (as seen above in their related scenarios 1 and 2), they have no real impact on the BER performance, that is little affected by the repetition (scheme 1) or alternation (scheme 2) of the information bits. Hence, although in principle the spreading sequences can be optimized, in practice the performance gain this optimization can provide in terms of BER is negligible. This can be theoretically justified by observing the power range in which Fig. 11 was obtained. At the optical power levels of interest, shot noise hardly ever impacts on system performance, so that $\sigma_0^2 \simeq \sigma_1^2$ can be safely assumed in (22), therefore the resulting mutual information does not depend on M_1 and other spreading schemes could possibly be adopted. For a given average received optical power, it is of course the spreading factor that strongly influences the BER. As expected, the performance scales linearly with the spreading factor size, so that a theoretical 3 dB improvement would be observed on the electrical signal power when the symbol period, i.e., M, is doubled. Instead, since results are drawn as a function of the optical power which is proportional (through the APD responsivity R) to the electrical signal amplitude, a 1.5 dB improvement can be observed when the spreading factor is doubled. Fig. 11 also reports the theoretical reference of the achievable mutual information (AMI), computed by resorting to (23).

Fig. 11 reports the BER performance only for the AWGN scenario while the stochastic fading due to turbulence is considered for the channel whose results are reported in Fig. 12, where the normalized variance of h, i.e., the so called power scintillation index (PSI), is equal to 0.1, amounting to weakly turbulent conditions. Even in this case, results were found to be insensitive to the adopted spreading scheme. Despite the expected performance degradation, with respect to the results on AWGN channel (also reported in figure for comparison), the BER curves for the fading channel are still parallel and evenly spaced, demonstrating that the same improvement by 1.5 dB, as in Fig. 11, applies every time the spreading factor is doubled.

B. Receiver With Variable Bandwidth

In the existing literature on LEO-DTE systems, some works discussing possible implementations of the VDR approach claim that a larger improvement, close to 3 dB, in terms of average received optical power can be obtained by doubling the symbol period [13]–[16]. Indeed, such a large and counter-intuitive gain relies on the physical features of the receiver front-end, assumed to consist in an APD followed by a TIA. Therein, as already outlined in Section IV-A, the feedback resistor plays the double role of dominant source of thermal noise, whose PSD (26) is inversely proportional to R_L, as well as of setting the receiver bandwidth B, which is again proportional to the inverse of R_L. Hence, the overall thermal noise power is proportional to R_L^{-2} and can be greatly attenuated by increasing the TIA feedback resistance, of course at the cost of a correspondingly decreased bandwidth.

Although the focus of this work is not on the optimization of receiver sensitivity, but rather on describing possible receiver architectures for the systems under investigation, along with their pros and cons, we report hereafter the enhanced gain that can be achieved by varying the TIA feedback resistance. Of course, this strategy is applicable only when the spreading scheme 1 is employed, since its choice is equivalent to an enlargement of the transmission pulse, and a corresponding reduction of its bandwidth by the spreading factor M, while the adoption of scheme 2 or of any other spreading scheme would leave the chip rate fixed at the maximum symbol rate, no matter how large M is. Fig. 13 shows the BER performance for an AWGN channel as well as for a channel with randomly turbulent fading when the value of the TIA feedback resistance is adapted to the used spreading factor M. For the largest value $M = 16$ considered in Fig. 13, the resulting $R_L \simeq 2.56$ kΩ still has a

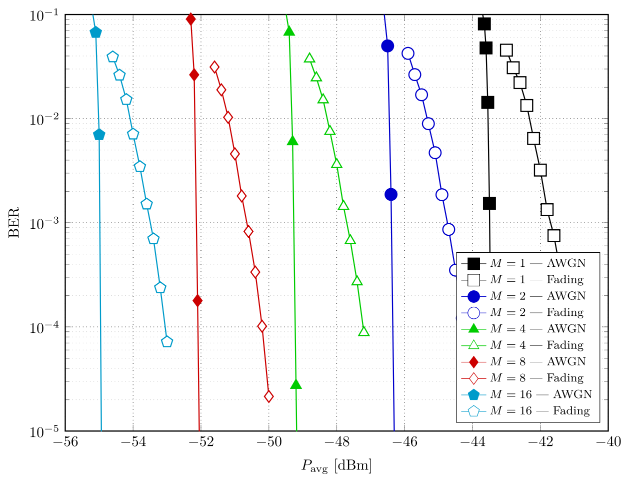

Fig. 13. BER performance on AWGN and turbulent fading channels, using the spreading scheme 1 and a receiver with adaptive bandwidth (and noisiness), for every M.

practical value. Regarding the practical implementation of a TIA with variable feedback resistance and bandwidth, there have been some studies in the literature as, e.g., [36] that discusses, among others, the switching speed of the device. In the present context, switching the TIA bandwidth is required only when the symbol rate, hence M, is changed, possibly because entering a different sector in the satellite orbit. If, however, the spreading scheme is changed between the preamble and the payload (so as to exploit the superior performance of spreading scheme 2 with respect to synchronization), then a switching of the TIA configuration would be required at every transmitted packet, which might exceed the affordable switching speed. We omit further discussions on the implementation of this solution, since they would go beyond the scope of this paper.

Results in Fig. 13 were obtained with the same code and power scintillation index as in Fig. 12 and demonstrate a 3 dB gain, in terms of average received optical power, at every doubling of the spreading factor. These results shall be used in the system level analysis that follows.

V. System Level Analysis

Given the complexity of the systems under investigation, we do not attempt to provide an analytical high-level model for a LEO-DTE VDR system (as done, e.g., in [17]) but rather resort to an analysis of the link budget. The purpose of the following system analysis is to highlight the significant benefits in terms of average throughput that stem from employing VDR instead of CDR. To this purpose, a discussion on the channel characteristics is necessary, so that a detailed link budget computation can be provided for a realistic scenario. A similar system analysis was partially presented in [37].

A. Channel Modeling and Link Variability

The first fundamental step for a system-level assessment is modelling the LEO-DTE optical channel. In particular, its dependency on the satellite elevation angle has to be accurately captured, since it is the key feature exploited by the VDR. The optical LEO-DTE link is assumed to be in cloud-free line-of-sight (CFLOS) conditions. Clouds may easily block optical signals, and OGS site diversity is needed to avoid the link disruption [38]. For simplicity, and as it is not expected to be an elevation dependent effect, pointing errors were not considered. Under these assumptions, the main atmospheric effects that degrade the LEO-DTE link are:

- atmospheric attenuation/transmittance;
- atmospheric turbulence due to changes in the refractive index.

The atmospheric turbulence induces a fading on the optical signal. The modified version of the Hufnagel-Valley model was used to represent the refractive index structure constant [39]. Concerning the fading statistics, in this paper the weak turbulence regime is used even for low elevation range, where the irradiance distribution may be approximated by a lognormal model [35]. To generate representative fading time series to be used in Section V-B, the synthesizer described in [37] was used. This synthesizer follows a methodology similar to the one presented in [35] and used in Section IV for generating a lognormal time series. A sequence of independent white Gaussian samples is filtered by a Butterworth low pass filter to introduce correlation, as the fading dynamics is obtained by tuning the filter cut-off (or Greenwood) frequency and the filter order. This tuning modifies the standard deviation of the output Gaussian process, which therefore needs to be renormalized. Finally, the desired statistics of the fading time series are induced by the choice of scintillation index, which drives the values of the parameters characterizing the lognormal distribution. In order to get a time series independent of the link budget, the average power of the final output must be normalized to unity. Finally, the values of scintillation loss reported is Table II correspond to an availability of 99.9%.

To understand the motivations for adopting a VDR transmission scheme, it is important to grasp how the channel effects may vary with the elevation angle. Table II depicts this variability assuming a wavelength of 1550 nm and an OGS located in Messina, Italy (latitude $= 38.1833\,°$N, longitude $= 15.55\,°$E, altitude $= 507$ m), that is used throughout this section as a realistic example. The OGS receives data from a LEO satellite on a polar orbit at 693 km altitude, very similar in orbital characteristics to Sentinel 1.[11] For this exercise, each pass of the LEO satellite over the OGS is split into six sectors with equal duration, corresponding to the elevation ranges $[5°, 7°]$, $[7°, 10°]$, $[10°, 15°]$, $[15°, 22°]$, $[22°, 37°]$, and $[37°, 90°]$. These sectors take into account the elevation distribution of the feasible elevation range between $5°$ and $90°$. However, not the whole range is covered in every satellite pass over the OGS location. For this particular satellite orbit and OGS location, a complete orbit cycle of 12 days was simulated, corresponding to 57 passes. The considered split of the possible elevation range defines six sectors of equal duration based on the overall elevation distribution. This eases the corresponding analysis and also the system operations. Of course, a change in the satellite orbit or in the OGS location would result in a different distribution of

[11] [Online]. Available: https://sentinel.esa.int/web/sentinel/missions/sentinel-1

TABLE II
CHANNEL MODELING AND LINK VARIABILITY

sector number	1	2	3	4	5	6	zenith
elevation range (°)	5-7	7-10	10-15	15-22	22-37	37-90	90
ref. elevation angle (°)	5	7	10	15	22	37	90
scintillation index	1.1881	0.6113	0.2899	0.1035	0.0369	0.0096	0.0058
Fried parameter (cm)	6.5	7.8	9.5	12.2	15.3	20.3	21.8
cutoff frequency (Hz)	88	71.3	57	43.7	33	24	22
atmospheric attenuation (dB)	2.6	1.9	1.4	0.9	0.6	0.4	0.3
scintillation loss (dB)	15.2	11.7	8.7	5.7	3.8	2.2	1.8
free space loss (dB)	266.3	265.7	264.8	263.4	261.6	258.7	255
total elevation-dependent loss (dB)	284.1	279.3	274.9	270	266	261.3	257.1

TABLE III
LINK BUDGET INCLUDING THE EFFECTS OF FEC CODING AND CHANNEL INTERLEAVING

sector number	1	2	3	4	5	6
elevation range (°)	5-7	7-10	10-15	15-22	22-37	37-90
satellite altitude (km)	693	693	693	693	693	693
link range (km)	2546.9	2372.8	2139.9	1819.8	1487.4	1066
Tx power (W)	0.1	0.1	0.1	0.1	0.1	0.1
Tx optical loss (dB)	3	3	3	3	3	3
Tx aperture (cm)	5	5	5	5	5	5
Tx antenna gain (dB)	99.2	99.2	99.2	99.2	99.2	99.2
Free space loss (dB)	266.3	265.7	264.8	263.4	261.6	258.7
atmospheric attenuation (dB)	2.6	1.9	1.4	0.9	0.6	0.4
cloud margin (dB)	3	3	3	3	3	3
Rx aperture (cm)	40	40	40	40	40	40
Rx antenna gain (dB)	117.1	117.1	117.1	117.1	117.1	117.1
Rx optical loss (dB)	3	3	3	3	3	3
Rx optical power (dBm)	-41.6	-40.3	-38.9	-37	-34.9	-31.8
SCCC code rate	0.46	0.46	0.46	0.46	0.46	0.46
symbol rate (Msym/s)	2500	5000	5000	10000	10000	10000
spreading factor	4	2	2	1	1	1
AWGN thresholds (dBm)	-49.2	-46.2	-46.2	-43.2	-43.2	-43.2
fading penalty margin (dB)	2.6	1.8	1	0.6	0.4	0
modem implementation loss (dB)	1	1	1	1	1	1
required optical power (dBm)	-45.6	-43.4	-44.2	-41.6	-41.8	-42.2
margin (dB)	4	3.1	5.3	4.6	6.9	10.4
offered data rate (Mbps)	1150	2300	2300	4600	4600	4600

elevation angle sectors. As expected, channel effects are harsher in the lower elevation ranges and become more benign as the elevation angle increases. From the last row of Table II, it is clear that the dependency on the elevation angle of the channel characteristics yields a total dynamic range of 27 dB (for this particular link). This very wide dynamic range is what the VDR aims at exploiting in order to bring the system throughput closer to its capacity bound by optimizing the symbol rate in each sector. Hence, the only parameter that is optimized, within each sector, is the spreading factor M, for which the smallest possible value is selected and from which stems the offered data rate.

B. Link Budget

To evaluate the average VDR and CDR system throughput during the pass, a link budget for each of the six sectors was calculated and reported in Table III. To derive the required sensitivity thresholds, the selected waveform was based on OOK with a SCCC with rate 0.46 as FEC code, and a convolutional channel interleaver with a duration of 450 ms. As mentioned in Section IV-B, the spreading scheme assumed for this analysis is the repetition scheme (scheme 1). It is worth highlighting that the results obtained in this analysis are not to be directly compared with the performance shown in Fig. 13: the fading profiles used here, as well as the size of the channel interleaver, are not the same as the one used in Section IV. Further details on the waveform and on the interleaver sizing can be found in [34]. The sensitivity thresholds required to decode the received signal were set equal to the corresponding theoretical thresholds for the AWGN channel shown in Fig. 13, plus an optimized fading penalty margin dependent on the elevation angle. The values chosen for this margin were proven in [37] to be sufficient to accommodate for the residual power penalty resulting by the combination of fading and channel interleaving. Indeed, most of the loss caused by the scintillation can be effectively recovered by suitably sized channel interleaver and FEC coding. While the

TABLE IV
AVERAGE SYSTEM THROUGHPUT FOR CDR AND VDR

Transmission scheme	**Average throughput** (Mbps)
CDR, from sector n.1	1150
CDR, from sector n.2	1916.7
CDR, from sector n.3	1533.3
CDR, from sector n.4	2300
CDR, from sector n.5	1533.3
CDR, from sector n.6	766.7
VDR	3258.3

channel interleaver decorrelates the fading realizations affecting a codeword, the FEC coding can correct the bits corrupted by the fading events. Therefore, the entry for the scintillation loss does not explicitly appear in Table III, but is implicitly accounted for by the fading penalty margin. On top of this fading penalty margin, an additional 1 dB margin was included to account for the modem implementation losses in real hardware. This value is representative of applications that are neither low-end (e.g., consumer Internet of things applications) nor very high-end (e.g., international scientific missions), and can encompass a broad range of optical LEO-DTE applications. Since a multi-mode fiber is assumed to deliver the received light to the APD, coupling losses were neglected [8]. The link budgets per sector resulting from these assumptions are presented in Table III, where the effects of FEC coding and channel interleaving are included. The criterion for declaring the link successfully closed is having a received optical power greater than the required optical power (both in bold in Table III) to achieve a target BER equal to 10^{-4} in a realistic implementation. The link budgets also yield the selection of the symbol rates, the resulting link margins (computed as the difference between the received optical powers and the required optical powers in Table III), and the offered data rates.

C. Average System Throughput Results

Using the sector link budgets in Table III, it is possible to compute and compare the average system throughput for both CDR and VDR. To optimize the CDR system throughput, Table IV presents six results for the CDR scheme. Each of these results is computed assuming that the transmission starts in a different sector, and that the link does not close in the preceding ones. Since CDR adopts one single symbol rate during the whole pass, it essentially trades a lower visibility time with a higher average throughput. Indeed, considering the six corresponding rows of Table IV, the best throughput for the CDR is obtained by initiating the transmission at sector 4 and transmitting at 4600 Mbps (as shown in column 4 in Table III) for 3/6 of the pass (i.e., during sectors 4, 5, and 6). The last row of Table IV shows the average throughput for the VDR, that was evaluated simply by averaging the offered data rates across the sectors, yielding 3258.3 Mbps. If compared to the best data return provided by the CDR scheme, it is clear that the VDR approach provides an improvement of 41.7% in terms of data return.

If a receiver with fixed bandwidth is used, as assumed in Section IV-A, then the alternating spreading scheme (scheme 2) can be considered. As shown in Fig. 12 by the spacing between the AWGN curves, the spreading gain would reduce to 1.5 dB, impacting significantly on the link budgets in Table III. With these assumptions, the VDR gain over the CDR would reduce to 29.2%. For brevity, these link budgets are omitted. These results highlight how the design of the spreading sequence and the receiver architecture may be seen as a trade-off between link budget quality and synchronization capability.

The throughput optimization procedure detailed in this Section illustrates a methodology, based on link budgeting, that depends on realistic system assumptions and that can be repeated when the OGS location or other relevant receiver characteristics (type of APD, code rate, etc.) are changed.

VI. CONCLUSION

The paper has addressed in depth the VDR technique implemented exclusively at the digital baseband layer, as a means to optimize transparently the data return of optical LEO DTE links employing OOK with an APD-based receiver over the whole elevation angle range. This was done by investigating both critical link level aspects, such as receiver synchronization performance, but also system level aspects, including channel modeling and link budget. Despite the throughput gain of VDR over CDR is very specific to a particular orbit, OGS location, spreading sequence, and receiver architecture, in general we showed how VDR can be used as a simple way to achieve a higher throughput and a longer visibility period. This capability, soon to be included in the CCSDS standard, will offer great flexibility to the next generation of optical LEO-DTE communications.

ACKNOWLEDGMENT

The authors would like to thank Lorenzo Gaudio for his precious help. Opinions, interpretations, recommendations, and conclusions presented in this paper are those of the authors and are not necessarily endorsed by ESA.

REFERENCES

[1] F. Heine, G. Mühlnikel, H. Zech, S. Philipp-May, and R. Meyer, "The European data relay system, high speed laser based data links," in *Proc. 7th Adv. Satell. Multimedia Syst. Conf./Proc. 13th Signal Proc. Space Commun. Workshop*, 2014, pp. 284–286.

[2] S. Müncheberg, C. Gal, J. Horwath, H. Kinter, L. M. Navajas, and M. Soutullo, "Development status and breadboard results of a laser communication terminal for large LEO constellations," in *Proc. Int. Conf. Space Opt.*, 2019, vol. 11180, pp. 1180–1192.

[3] C. Fuchs, F. Moll, D. Giggenbach, C. Schmidt, J. Keim, and S. Gaisser, "OSIRISv1 on flying laptop: Measurement results and outlook," in *Proc. IEEE Int. Conf. Space Opt. Syst. Appl.*, 2019, pp. 1–5.

[4] F. Moll, "Experimental analysis of channel coherence time and fading behavior in the LEO-ground link," in *Proc. Int. Conf. Space Opt. Syst. Appl.*, 2014, pp. S4-2.1-7.

[5] D. Giggenbach and H. Henniger, "Fading-loss assessment in atmospheric free-space optical communication links with on-off keying," *Opt. Eng.*, vol. 47, no. 4, 2008, Art. no. 046001.

[6] N. Toptsidis, P.-D. Arapoglou, and M. Bertinelli, "Link adaptation for Ka band low Earth orbit Earth observation systems: A realistic performance assessment," *Int. J. Satell. Commun. Netw.*, vol. 30, no. 3, pp. 131–146, May 2012.

[7] T. Ito, Y. Ono, Y. Hasegawa, and M. Arikawa, "Experimental evaluation of adaptive distributed frame repetition at 10 Gbps for the satellite-to-ground optical link," in *Proc. Int. Conf. Space Opt.*, 2019, vol. 11180, pp. 2087–2093.
[8] C. M. Schieler, A. S. Garg, B. C. Bilyeu, J. P. Wang, and B. S. Robinson, "Demonstration of reliable high-rate optical communication over an atmospheric link using ARQ," in *Proc. IEEE Int. Conf. Space Opt. Syst. Appl.*, 2019, pp. 1–6.
[9] B. S. Robinson, C. M. Schieler, and D. M. Boroson, "Large-volume data delivery from low-Earth orbit to ground using efficient single-mode optical receivers," in *Proc. Free-Space Laser Commun. Atmosph. Propag. XXVIII*, H. Hemmati and D. M. Boroson, Eds., 2016, vol. 9739, pp. 74–81.
[10] C. M. Schieler *et al.*, "NASA's terabyte infrared delivery (TBIRD) program: Large-volume data transfer from LEO," in *Proc. 33rd Annu. AIAA/USU Conf. Small Satellites*, 2019, pp. SS C19–VI–02.
[11] D. J. Geisler, C. M. Schieler, T. M. Yarnall, M. L. Stevens, B. S. Robinson, and S. A. Hamilton, "Demonstration of a variable data-rate free-space optical communication architecture using efficient coherent techniques," *Opt. Eng.*, vol. 55, no. 11, pp. 1–12, 2016.
[12] D. O. Caplan, B. S. Robinson, R. J. Murphy, and M. L. Stevens, "Demonstration of 2.5-Gslot/s optically-preamplified M-PPM with 4 photons/bit receiver sensitivity," in *Proc. Opt. Fiber Commun. Conf. Expo. Nat. Fiber Optic Engineers Conf.*, 2005, Paper PD P32.
[13] N. W. Spellmeyer *et al.*, "A multi-rate DPSK modem for free-space laser communications," in *Proc. Free-Space Laser Commun. Atmosph. Propag. XXVI*, H. Hemmati and D. M. Boroson, Eds., Bellingham, WA, USA, 2014, vol. 8971, pp. 130–138.
[14] D. O. Caplan *et al.*, "Multi-rate DPSK optical transceivers for free-space applications," in *Proc. Free-Space Laser Commun. Atmosph. Propag. XXVI*, H. Hemmati and D. M. Boroson, Eds., Bellingham, WA, USA, 2014, vol. 8971, pp. 139–151.
[15] J. P. Wang *et al.*, "Performance and qualification of a multi-rate DPSK modem," in *Proc. Free-Space Laser Commun. Atmosph. Propag. XXVI*, H. Hemmati and D. M. Boroson, Eds., Bellingham, WA, USA, 2014, vol. 8971, pp. 302–310.
[16] D. M. Hall, R. K. DeLong, D. G. Heflinger, and P. M. Tanner, "Multi-rate variable duty cycle modem for use in an optical communication system," U.S. Patent 6 661 975B1, Dec. 2003. [Online]. Available: https://patents.google.com/patent/US6661975B1/en
[17] N. Perlot and T. de Cola, "Throughput maximization of optical LEO-ground links," in *Proc. Free-Space Laser Commun. Technol. XXIV*, H. Hemmati and D. M. Boroson, Eds., Bellingham, WA, USA, 2012, vol. 8246, Art. no. 82460V.
[18] W. G. Cowley, K. D. Nguyen, and D. Giggenbach, "Adaptive symbol-rate free-space-optical communications," in *Proc. Australian Commun. Theory Workshop*, 2013, pp. 122–127.
[19] A. Shrestha and D. Giggenbach, "Variable data rate for optical low-Earth-orbit (LEO) downlinks," in *Proc. Photon. Netw.; 17. ITG Symp.*, 2016, pp. 1–5.
[20] J. Pacheco-Labrador, A. Shrestha, J. C. R. Molina, and D. Giggenbach, "Implementation of variable data rates in transceiver for free-space optical LEO to ground link," in *Proc. Environ. Effects Light Propag. Adaptive Syst. III*, K. Stein and S. Gladysz, Eds., Bellingham, WA, USA, 2020, vol. 11532, pp. 90–98.
[21] G. Agrawal, *Fiber-Optic Communications Systems*, 3rd ed., Hoboken, NJ, USA: Wiley, 2002.
[22] E. Hall and S. Wilson, "Convolutional interleavers for stream-oriented parallel concatenated convolutional codes," in *Proc. IEEE Int. Symp. Inf. Theory*, 1998, p. 33.
[23] M. Morelli, M. Moretti, A. A. D'Amico, and G. Colavolpe, "Frame synchronization for FSO links with unknown signal amplitude and noise power," *IEEE Wireless Commun. Lett.*, vol. 10, no. 7, pp. 1498–1502, Jul. 2021.
[24] U. Mengali and A. N. D'Andrea, *Synchronization Techniques for Digital Receivers*, (Applications of Communications Theory). New York, NY, USA: Plenum, 1997.
[25] M. Cohn and A. Lempel, "On fast M-sequence transforms," *IEEE Trans. Inf. Theory*, vol. 23, no. 1, pp. 135–137, Jan. 1977.
[26] J. D. H. Alexander, "Clock recovery from random binary signals," *IEE Electron. Lett.*, vol. 11, pp. 541–542, Oct. 1975.
[27] C. Hogge, "A self correcting clock recovery circuit," *IEEE Trans. Electron Devices*, vol. 32, no. 12, pp. 2704–2706, Dec. 1985.
[28] D. T. Nguyen and Y. Park, "Performance analysis of interleaved LDPC for optical satellite communications," *Opt. Commun.*, vol. 442, pp. 13–18, 2019.
[29] *Pink Sheets for Optical Communications Coding and Synchronization*, CCSDS, 142.0-B-1, Aug. 2021.
[30] T. M. Cover and J. A. Thomas, *Elements of Information Theory*, 2nd ed., New York, NY, USA: Wiley, 2006.
[31] I. Ali, N. Al-Dhahir, and J. E. Hershey, "Doppler characterization for LEO satellites," *IEEE Trans. Commun.*, vol. 46, no. 3, pp. 309–313, Mar. 1998.
[32] G. T. Buračas and G. M. Boynton, "Efficient design of event-related fMRI experiments using M-sequences," *NeuroImage*, vol. 16, no. 3, Part A, pp. 801–813, 2002. [Online]. Available: https://www.sciencedirect.com/science/article/pii/S105381190291116X
[33] K. Kiasaleh, "Receiver architecture for channel-aided, OOK, APD-based FSO communications through turbulent atmosphere," *IEEE Trans. Commun.*, vol. 63, no. 1, pp. 186–194, Jan. 2015.
[34] N. Mazzali and P.-D. Arapoglou, "Channel interleaver dimensioning for optical LEO direct-to-earth systems," in *Proc. 10th Adv. Satell. Multimedia Syst. Conf./Proc. 16th Signal Process. Space Commun. Workshop*, 2020, pp. 1–6.
[35] D. Giggenbach, A. Shrestha, F. Moll, C. Fuchs, and K. Saucke, "Reference power vectors for the optical LEO downlink channel," in *Proc. IEEE Int. Conf. Space Opt. Syst. Appl.*, 2019, pp. 1–4.
[36] S. Deng, E. Cleary, M. A. McAuliffe, and L. Lewis, "Design of an auto-gain control transimpedance amplifier for optical sensing applications," in *Proc. 27th Ir. Signals Syst. Conf.*, 2016, pp. 1–5.
[37] P.-D. Arapoglou and N. Mazzali, "System-level benefit of variable data rate in optical LEO direct-to-earth links," in *Proc. Int. Conf. Space Opt.*, 2021, Art. no. 118524I.
[38] N. Lyras, C. Efrem, C. Kourogiorgas, A. Panagopoulos, and P.-D. Arapoglou, "Optimizing the ground network of MEO optical satellite communication systems," *IEEE Syst. J.*, vol. 14, no. 3, pp. 3968–3976, Sep. 2020.
[39] L. C. Andrews and R. L. Phillips, *Laser Beam Propagation Through Random Media*, 2nd ed., Bellingham, WA, USA: SPIE, 2005.

Pantelis-Daniel Arapoglou received the Diploma in electrical and computer engineering and the Dr. Eng. degree from the National Technical University of Athens (NTUA), Athens, Greece, in 2003 and 2007, respectively. From 2008 to 2010, he was involved in postdoctoral research on MIMO over satellite jointly supported by the NTUA and the European Space Agency Research and Technology Centre (ESA/ESTEC), Noordwijk, The Netherlands. From 2010 to 2011, he was a Research Associate with the Interdisciplinary Centre for Security, Reliability and Trust (SnT), University of Luxembourg, Luxembourg, Luxembourg. Since 2011, he has been a Communications System Engineer with ESA/ESTEC, where he is technically supporting ESA missions, such as HydRON (High Throughput Optical Network) and European Data Relay Satellite (EDRS), and also research and development activities in the areas of satellite telecommunications, digital, and optical communications.

Giulio Colavolpe (Senior Member, IEEE) received the Dr.Ing. degree (*cum laude*) in telecommunications engineering from the University of Pisa, Pisa, Italy, in 1994, and the Ph.D. degree in information technologies from the University of Parma, Parma, Italy, in 1998. Since 1997, he has been with the University of Parma, where he is currently a Professor of telecommunications with the Dipartimento di Ingegneria e Architettura. In 2000, he was a Visiting Scientist with Institut Eurécom, Valbonne, France. In 2013, he was a Visiting Scientist with the European Space Agency (ESTEC), Noordwijk, The Netherlands. His research interests include the design of digital communication systems, adaptive signal processing, with particular emphasis on iterative detection techniques for channels with memory, channel coding, and information theory. His research activity has led to more than 200 papers in refereed journals and in leading international conferences, and 18 industrial patents. He was the recipient of the Best Paper Award at the 13th International Conference on Software, Telecommunications, and Computer Networks (SoftCOM'05), Split, Croatia, September 2005, Best Paper Award for Optical Networks and Systems at the IEEE International Conference on Communications (ICC 2008), Beijing, China, in May 2008, and Best Paper Award at the fifth Advanced Satellite Mobile Systems Conference and 11th International Workshop on Signal Processing for Space Communications (ASMS&SPSC 2010), Cagliari, Italy. He was the Editor of IEEE TRANSACTIONS ON WIRELESS COMMUNICATIONS, IEEE TRANSACTIONS ON COMMUNICATIONS, and IEEE WIRELESS COMMUNICATIONS LETTERS, and the Executive Editor of *Transactions on Emerging Telecommunications Technologies*.

Tommaso Foggi received the master's degree in telecommunication engineering and the Ph.D. degree in information technology from the University of Parma, Parma, Italy, in 2003 and 2008, respectively. From 2009 to 2018, he was a Research Engineer with the Research Unit of National Inter-University Consortium for Telecommunications, University of Parma. He is currently an Associate Professor with the Department of the Engineering and Architecture, University of Parma. His main research interests include electronic signal processing for optical and satellite communication systems. He is the author of tens of peer-reviewed papers and several patents. He was the recipient of the Best Paper Award in the Optical Networks and Systems Symposium at the IEEE International Conference on Communications (ICC 2008), Beijing, China, May 2008. He was/is involved in many research projects funded by public authorities, such as MIUR, ESA, EU or private companies, such as Ericsson, CGS, Inmarsat, and Huawei.

Nicolò Mazzali (Member, IEEE) received the master's degree (*cum laude*) in telecommunications engineering and the Ph.D. degree in information technologies from the University of Parma, Parma, Italy, in 2009 and 2013, respectively. He was a Visiting Postdoctoral Researcher with the Department of Signals and Systems, Chalmers University of Technology, Gothenburg, Sweden, and a Research Associate with the Interdisciplinary Centre for Security, Reliability and Trust, University of Luxembourg, Luxembourg. Since 2018, he has been a Communication Systems and Technologies Engineer with the Directorate of Technology, Engineering, and Quality, European Space Agency. His research interests include signal processing for wireless, satellite, and free-space optical communications, synchronization, and estimation theory.

Armando Vannucci received the Dr.Ing. degree in electronic engineering (*cum laude*) from the University of Rome (La Sapienza), Rome, Italy, in 1993, discussing a thesis about the digital analysis of speech signals applied to speech recognition, and the Ph.D. degree in information technology from the University of Rome, Rome, Italy. During 1993–1994, he was with Department of INFO-COM, University of Rome and during 1995–1998, as a Ph.D. Student, he joined an industrial research project on digital radio links, for which he holds two patents with the University of Parma, discussing the thesis Sequence estimation receivers for nonlinear transmission channels with the Polytechnic of Turin, Turin, Italy. From 1998 to 2002, he held various positions with the University of Parma, where he became an Assistant Professor in 2002. His research interests included variational techniques for the design of digital receivers; fiber optics transmission, polarization mode dispersion, optical amplifiers, and digital speech processing. He took part in various research projects, both institutional and with industrial partners. He is the author of more than 50 scientific publications, mostly on international journals (40%), conference proceedings, books, book chapters, and patents. He was a Visiting Scientist with Alcatel Labs, Marcoussis, France, and with Université Laval, Québec City, QC, Canada, and a Visiting Lecturer with Hochschule Karlsruhe, Germany. He is the author of two textbooks and has taught several courses (undergraduate, graduate, master, Ph.D., summer schools) with the Universities of Rome, Urbino, and Parma, where he is currently In-charge of Signals and Systems.